Enhanced muonization by active-sterile neutrino mixing in protoneutron stars

Anupam Ray[1,2,*] and Yong-Zhong Qian[2,†]

[1]*Department of Physics, University of California Berkeley, Berkeley, California 94720, USA*
[2]*School of Physics and Astronomy, University of Minnesota, Minneapolis, Minnesota 55455, USA*

(Received 23 April 2024; accepted 9 July 2024; published 2 August 2024)

We study ν_μ-ν_s and $\bar{\nu}_\mu$-$\bar{\nu}_s$ mixing in the protoneutron star (PNS) created in a core-collapse supernova (CCSN). We point out the importance of the feedback on the general composition of the PNS in addition to the obvious feedback on the ν_μ lepton number. We show that for our adopted mixing parameters $\delta m^2 \sim 10^2$ keV^2 and $\sin^2 2\theta$ consistent with the current constraints, sterile neutrino production is dominated by the Mikheyev–Smirnov–Wolfenstein conversion of $\bar{\nu}_\mu$ into $\bar{\nu}_s$ and that the subsequent escape of $\bar{\nu}_s$ increases the ν_μ lepton number, which in turn enhances muonization of the PNS primarily through $\nu_\mu + n \to p + \mu^-$. While these results are qualitatively robust, their quantitative effects on the dynamics and active neutrino emission of core-collapse supernovae should be evaluated by including ν_μ-ν_s and $\bar{\nu}_\mu$-$\bar{\nu}_s$ mixing in the simulations.

DOI: 10.1103/PhysRevD.110.043007

I. INTRODUCTION

Sterile neutrinos (ν_s) associated with a vacuum mass eigenstate of keV-scale mass are a viable candidate for the mysterious dark matter [1–5]. Because of their tiny mixing with active neutrinos (ν_α), they can decay radiatively, $\nu_s \to \nu_\alpha + \gamma$, thereby allowing experimental probes through the decay x-ray line. In fact, major experimental constraints on active-sterile neutrino mixing primarily come from such x-ray searches [6–11]. There are also other significant constraints from phase-space considerations (the Tremaine-Gunn bound) [12–15], measurement of Lyman-α forests [16–18], and terrestrial nuclear decay searches [19–22]. Among many theoretical explorations, a number of studies have investigated the effects of active-sterile neutrino mixing in core-collapse supernovae (CCSNe) [23–37]. In this paper, we focus on the mixing between ν_μ ($\bar{\nu}_\mu$) and ν_s ($\bar{\nu}_s$) with a vacuum mass-squared difference of $\delta m^2 \sim 10^2$ keV^2 in protoneutron stars (PNSs) created in CCSNe. In particular, we treat this mixing in the presence of muons. In contrast to Ref. [34], which focused on the energy loss due to ν_x-ν_s and $\bar{\nu}_x$-$\bar{\nu}_s$ ($x = \mu, \tau$) mixing and stated that the presence of muons makes little difference, we show that inclusion of muons leads to more complicated feedback effects for ν_μ-ν_s and $\bar{\nu}_\mu$-$\bar{\nu}_s$ mixing than those for ν_τ-ν_s and $\bar{\nu}_\tau$-$\bar{\nu}_s$ mixing.

Owing to the high densities and temperatures in the PNS, muon production or muonization (e.g., $e^- + \bar{\nu}_e \to \mu^- + \bar{\nu}_\mu$, $\nu_\mu + n \to p + \mu^-$) is energetically allowed and dynamically important for the neutrino-driven explosion [38]. The dynamic effects of muonization can be understood qualitatively as follows. For the conditions in the PNS, electrons are highly relativistic, and their contribution to the pressure is $\approx 1/3$ of their energy density. Without muons, charge neutrality requires an equal number of electrons and protons. For a given initial distribution of protons, as some electrons are converted into muons, a fraction of the electron energy is converted into the rest mass energy of muons, thereby reducing the net pressure. Consequently, the PNS contracts faster, and the resulting increase in neutrino luminosity enhances heating of the material outside the PNS, which helps the neutrino-driven explosion [38]. The conditions in the PNS also facilitate conversion of $\bar{\nu}_\mu$ into $\bar{\nu}_s$ through the Mikheyev–Smirnov–Wolfenstein (MSW) effect [39,40], which tends to increase the ν_μ lepton number, thereby enhancing muonization mainly through the reaction $\nu_\mu + n \to p + \mu^-$. While the corresponding dynamic effects must be investigated by incorporating ν_μ-ν_s and $\bar{\nu}_\mu$-$\bar{\nu}_s$ mixing in CCSN simulations, our goal in this paper is to illustrate how such mixing enhances muonization in the PNS and to estimate the potential enhancement.

The rest of the paper is organized as follows. In Sec. II we discuss the production of sterile neutrinos through ν_μ-ν_s

*Contact author: anupam.ray@berkeley.edu
†Contact author: qianx007@umn.edu

Published by the American Physical Society under the terms of the Creative Commons Attribution 4.0 International license. Further distribution of this work must maintain attribution to the author(s) and the published article's title, journal citation, and DOI. Funded by SCOAP³.

and $\bar{\nu}_\mu$-$\bar{\nu}_s$ mixing in a PNS. Much of the treatment is similar to that of ν_τ-ν_s and $\bar{\nu}_\tau$-$\bar{\nu}_s$ mixing, and we closely follow the discussion in Ref. [35]. In Sec. III we discuss the treatment of the feedback effects of ν_μ-ν_s and $\bar{\nu}_\mu$-$\bar{\nu}_s$ mixing in the presence of muons. In Sec. IV we present example calculations to illustrate the effects of such mixing on muonization in the PNS. In Sec. V we discuss our results and give conclusions.

II. PRODUCTION OF STERILE NEUTRINOS IN A PNS

We assume spherical symmetry, for which the conditions in the PNS are functions of radius r and time t only. We focus on the region where all active neutrinos are diffusing and assume that all particles of concern, n, p, $e^\pm$, $\mu^\pm$, ν_e, $\bar{\nu}_e$, ν_μ, $\bar{\nu}_\mu$, ν_τ, and $\bar{\nu}_\tau$, have Fermi-Dirac energy distributions characterized by the same temperature T but species-specific chemical potentials. For example, the ν_μ and $\bar{\nu}_\mu$ energy distributions (number densities per unit energy interval per unit solid angle) are

$$\frac{d^2 n_{\nu_\mu}}{dE d\Omega} = \frac{1}{(2\pi)^3} \frac{E^2}{\exp[(E-\mu_{\nu_\mu})/T]+1}, \tag{1a}$$

$$\frac{d^2 n_{\bar{\nu}_\mu}}{dE d\Omega} = \frac{1}{(2\pi)^3} \frac{E^2}{\exp[(E+\mu_{\nu_\mu})/T]+1}, \tag{1b}$$

where μ_{ν_μ} is the ν_μ chemical potential, and we have used $\mu_{\bar{\nu}_\mu} = -\mu_{\nu_\mu}$. The corresponding ν_μ lepton number fraction (net number per baryon) is

$$Y_{\nu_\mu} = \frac{n_{\nu_\mu} - n_{\bar{\nu}_\mu}}{n_b} = \frac{T^3 \eta_{\nu_\mu}}{6 n_b}\left(1 + \frac{\eta_{\nu_\mu}^2}{\pi^2}\right), \tag{2}$$

where $\eta_{\nu_\mu} = \mu_{\nu_\mu}/T$ and n_b is the baryon number density.

The treatment of ν_μ-ν_s and $\bar{\nu}_\mu$-$\bar{\nu}_s$ mixing would mirror that of ν_τ-ν_s and $\bar{\nu}_\tau$-$\bar{\nu}_s$ mixing (e.g., [27,28,31,32,34,35]) were there no muons. With muons, the effective potential for ν_μ-ν_s mixing is

$$V_\nu = \sqrt{2} G_F n_b \left(-\frac{Y_n}{2} + Y_\mu + Y_{\nu_e} + 2Y_{\nu_\mu}\right), \tag{3}$$

where G_F is the Fermi constant, and Y_α ($\alpha = n$, μ, ν_e, and ν_μ) is the net number fraction for species α. In Eq. (3), we have applied the constraint of charge neutrality, $Y_e + Y_\mu = Y_p$, so the contributions from forward scattering of ν_μ on protons and electrons do not appear explicitly. We have also assumed that there is no net ν_τ lepton number in the PNS (i.e., $Y_{\nu_\tau} = 0$ and $\mu_{\nu_\tau} = 0$). Note that V_ν, n_b, and Y_α are all functions of r and t. For convenience, here and below, we usually suppress such radial and temporal dependence. The potential for $\bar{\nu}_\mu$-$\bar{\nu}_s$ mixing is $V_{\bar{\nu}} = -V_\nu$.

The potential V_ν ($V_{\bar{\nu}}$) modifies the mixing angle between ν_μ ($\bar{\nu}_\mu$) and ν_s ($\bar{\nu}_s$) in the PNS. For ν_μ and $\bar{\nu}_\mu$ with energy E, the effective mixing angles are given by

$$\sin^2 2\theta_\nu = \frac{\Delta^2 \sin^2 2\theta}{(\Delta \cos 2\theta - V_\nu)^2 + \Delta^2 \sin^2 2\theta}, \tag{4a}$$

$$\sin^2 2\theta_{\bar{\nu}} = \frac{\Delta^2 \sin^2 2\theta}{(\Delta \cos 2\theta - V_{\bar{\nu}})^2 + \Delta^2 \sin^2 2\theta}, \tag{4b}$$

where $\theta \ll 1$ is the vacuum mixing angle and $\Delta = \delta m^2/(2E)$. For the conditions in the PNS, $V_\nu < 0$ and $V_{\bar{\nu}} > 0$. Therefore, ν_μ-ν_s mixing is suppressed whereas $\bar{\nu}_\mu$-$\bar{\nu}_s$ mixing can be enhanced by the MSW resonance. This resonance occurs when $\Delta \cos 2\theta = V_{\bar{\nu}}$, and defines a resonance energy $E_R = \delta m^2 \cos 2\theta/(2V_{\bar{\nu}})$.

Resonant conversion of $\bar{\nu}_\mu$ into $\bar{\nu}_s$ is the dominant mechanism for producing sterile neutrinos inside the PNS (e.g., [31,32,34,35]). We follow Ref. [35] and adopt the following rate of change in Y_{ν_μ} due to the MSW conversion of $\bar{\nu}_\mu$ and the subsequent escape of $\bar{\nu}_s$ from the PNS:

$$\dot{Y}_{\nu_\mu}^{\rm MSW} = \Theta(\lambda_R - \delta r) \frac{\pi E_R (1 - P_{\rm LZ}^2)}{n_b H_R} \left.\frac{d^2 n_{\bar{\nu}_\mu}}{dE d\Omega}\right|_{E_R}. \tag{5}$$

In the above equation, $\Theta(x)$ is the Heaviside step function, $\lambda_R = 1/[n_b \sigma(E_R)]$ is the mean free path at the resonant neutrino energy E_R, $\sigma(E) \approx G_F^2 E^2/\pi$ is the cross section governing $\bar{\nu}_\mu$ diffusion (e.g., [28]), $\delta r = 2H_R \tan 2\theta$ is the width of the resonance region, H_R is the scale height $|\partial \ln V_{\bar{\nu}}/\partial r|^{-1}_{E_R}$ with the derivative taken at the resonance radius for E_R, and

$$P_{\rm LZ} = \exp\left(-\frac{\pi \delta m^2 H_R \sin^2 2\theta}{4 E_R \cos 2\theta}\right) \tag{6}$$

is the Landau-Zener survival probability for a radially propagating $\bar{\nu}_\mu$ after it crosses the resonance. Note that a radially outgoing $\bar{\nu}_\mu$ crosses the resonance only once, whereas a radially incoming $\bar{\nu}_\mu$ crosses the resonance twice (see Fig. 1). Both situations are taken into account [35] by Eq. (5).

Apart from the MSW conversion of $\bar{\nu}_\mu$ into $\bar{\nu}_s$, ν_s ($\bar{\nu}_s$) can be produced via collisions of ν_μ ($\bar{\nu}_\mu$) with the PNS constituents. In this scenario, ν_μ ($\bar{\nu}_\mu$) evolves as a linear combination of two effective mass eigenstates between collisions. Upon collision, which is predominantly with baryons, the wave function collapses, and a ν_s ($\bar{\nu}_s$) is produced with a probability proportional to $\sin^2 2\theta_\nu$ ($\sin^2 2\theta_{\bar{\nu}}$). For the mixing parameters of interest, the collisional production of ν_s and $\bar{\nu}_s$ inside a PNS is much less efficient than the MSW conversion of $\bar{\nu}_\mu$ into $\bar{\nu}_s$.

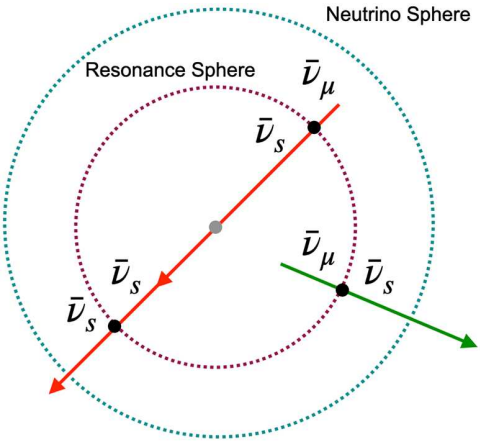

FIG. 1. Illustration of two types of escaping $\bar{\nu}_s$. One type is converted from radially outgoing $\bar{\nu}_\mu$ that experience a single MSW resonance, while the other type is converted from radially incoming $\bar{\nu}_\mu$ that experience two resonances (with conversion occurring only at the first resonance).

Nevertheless, for completeness, we also include the following contribution in the rate of change in Y_{ν_μ} from the collisional production of ν_s and $\bar{\nu}_s$:

$$\dot{Y}^{\rm coll}_{\nu_\mu} = G_F^2\left(\int_{E_{\bar{\nu}_\mu}} dE\, E^2 \sin^2 2\theta_{\bar{\nu}} \frac{d^2 n_{\bar{\nu}_\mu}}{dE d\Omega} - \int_0^\infty dE\, E^2 \sin^2 2\theta_{\nu} \frac{d^2 n_{\nu_\mu}}{dE d\Omega}\right). \tag{7}$$

In the above equation, the integration over $E_{\bar{\nu}_\mu}$ excludes the range $[E_R - \delta E/2, E_R + \delta E/2]$ with $\delta E = (\lambda_R/H_R)E_R$ when λ_R exceeds δr and MSW conversion occurs for resonant $\bar{\nu}_\mu$, but covers the entire energy range otherwise.

III. FEEDBACK FROM ACTIVE-STERILE NEUTRINO MIXING

We focus on the region where active neutrinos are trapped. Because sterile neutrinos can escape from this region, ν_μ-ν_s and $\bar{\nu}_\mu$-$\bar{\nu}_s$ mixing leads to changes of the ν_μ and $\bar{\nu}_\mu$ energy distributions, which in turn cause evolution of Y_{ν_μ}, and hence that of V_ν and $V_{\bar{\nu}}$. This type of feedback also occurs for ν_τ-ν_s and $\bar{\nu}_\tau$-$\bar{\nu}_s$ mixing [28,32,34,35]. What is new here, however, is that the changes of the ν_μ and $\bar{\nu}_\mu$ energy distributions cause evolution of Y_n, Y_p, and Y_μ through the reactions

$$\nu_\mu + n \to p + \mu^-, \tag{8a}$$

$$\bar{\nu}_\mu + p \to n + \mu^+. \tag{8b}$$

Therefore, the feedback effects for ν_μ-ν_s and $\bar{\nu}_\mu$-$\bar{\nu}_s$ mixing are more complicated than those for ν_τ-ν_s and $\bar{\nu}_\tau$-$\bar{\nu}_s$ mixing. Reactions in Eqs. (8a) and (8b) also occur in reverse, and there are parallel processes involving ν_e and $\bar{\nu}_e$ as well:

$$\nu_e + n \rightleftharpoons p + e^-, \tag{9a}$$

$$\bar{\nu}_e + p \rightleftharpoons n + e^+. \tag{9b}$$

Consequently, in order to treat the feedback on V_ν and $V_{\bar{\nu}}$ for ν_μ-ν_s and $\bar{\nu}_\mu$-$\bar{\nu}_s$ mixing, we must include all the processes described above to follow the evolution of Y_n, Y_p, Y_μ, Y_e, Y_{ν_μ}, and Y_{ν_e} simultaneously.

As mentioned in Sec. II, the particles of concern, n, p, $\mu^\pm$, $e^\pm$, ν_μ, $\bar{\nu}_\mu$, ν_e, and $\bar{\nu}_e$, are assumed to have Fermi-Dirac energy distributions characterized by the same temperature T but species-specific chemical potentials. For fixed T and n_b, the number fractions Y_n, Y_p, Y_μ, Y_e, Y_{ν_μ}, and Y_{ν_e} are specified by the corresponding chemical potentials [see, e.g., Eq. (2) for Y_{ν_μ}]. We use the following six constraints to determine these chemical potentials:

$$Y_n + Y_p = 1, \tag{10a}$$

$$Y_e + Y_\mu = Y_p, \tag{10b}$$

$$\mu_{\nu_e} + \mu_n = \mu_p + \mu_e, \tag{10c}$$

$$\mu_{\nu_\mu} + \mu_n = \mu_p + \mu_\mu, \tag{10d}$$

$$\dot{Y}_e + \dot{Y}_{\nu_e} = \Gamma_{L_e}, \tag{10e}$$

$$\dot{Y}_\mu + \dot{Y}_{\nu_\mu} = \Gamma_{L_\mu}, \tag{10f}$$

where Γ_{L_e} and Γ_{L_μ} are the net rates of change in $Y_e + Y_{\nu_e}$ and $Y_\mu + Y_{\nu_\mu}$ (see below). The constraints in Eqs. (10a), (10b), (10e), and (10f) correspond to conservation of baryon number, electric charge, and net lepton numbers of the electron and muon types. We have assumed that chemical equilibrium is achieved among n, p, $e^\pm$, ν_e, and $\bar{\nu}_e$ [Eq. (10c)], and also among n, p, $\mu^\pm$, ν_μ, and $\bar{\nu}_\mu$ [Eq. (10d)]. This assumption is consistent with the Fermi-Dirac energy distributions adopted for the above particles and with the fast rates (see Appendix) for interconverting n and p by these particles.

For the net rates of change in $Y_e + Y_{\nu_e}$ and $Y_\mu + Y_{\nu_\mu}$, we ignore the transport of Y_{ν_e} and Y_{ν_μ} by diffusion and take

$$\Gamma_{L_e} = 0, \tag{11a}$$

$$\Gamma_{L_\mu} = \dot{Y}^{\rm MSW}_{\nu_\mu} + \dot{Y}^{\rm coll}_{\nu_\mu}. \tag{11b}$$

The above approximation highlights the effects of sterile neutrino production, and its validity will be discussed in Sec. V.

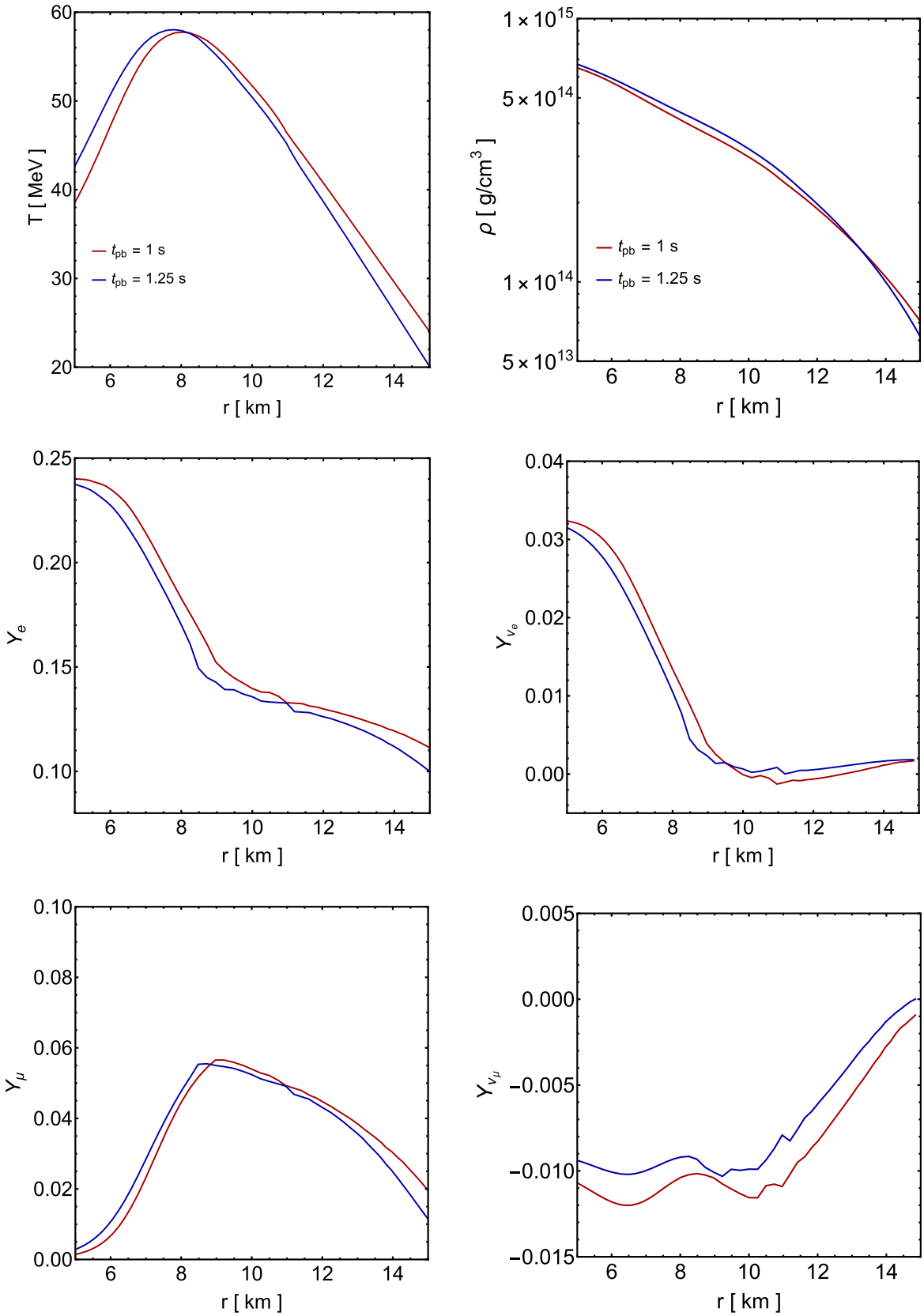

FIG. 2. Comparison of the radial profiles of T, ρ, Y_e, Y_{ν_e}, Y_μ, and Y_{ν_μ} at $t_{\rm pb} = 1$ and 1.25 s for a $20M_\odot$ CCSN model (with the SFHo nuclear equation of state and with muonization) provided by the Garching group [38,41].

IV. RESULTS

We now present example calculations of the effects of ν_μ-ν_s and $\bar{\nu}_\mu$-$\bar{\nu}_s$ mixing in a PNS. We expect that in addition to the feedback effects discussed in Sec. III, such mixing would also affect the evolution of temperature T and density ρ. As mentioned in the Introduction, such dynamic effects can be properly quantified only by including ν_μ-ν_s and $\bar{\nu}_\mu$-$\bar{\nu}_s$ mixing in CCSN simulations. Our goal here, however, is to elucidate how such mixing enhances muonization. As a reasonable approximation, we limit the duration of our calculations so that the radial profiles of T and ρ can be considered as fixed in time. As the initial conditions, we take a snapshot at time post bounce $t_{\rm pb} = 1$ s of a $20M_\odot$ CCSN model (with the SFHo nuclear equation of state and with muonization) provided by the Garching group [38,41]. Based on the comparison of the conditions at $t_{\rm pb} = 1$ s and those at the next output instant $t_{\rm pb} = 1.25$ s (see Fig. 2), we consider it reasonable to assume no evolution of $T(r)$ and $\rho(r)$ for a duration of $\Delta t = 0.1$ s. We also limit our calculations to within the radius $r = 14.7$ km, which corresponds to a temperature of $T = 25.6$ MeV and a density of $\rho = 8.01 \times 10^{13}$ g cm^{-3}, so that all active neutrinos are in the trapped regime throughout the calculations.

Starting with the conditions at $t_{\rm pb} = 1$ s and taking $T(r)$ and $\rho(r)$ as fixed in time, we follow the evolution of Y_n, Y_p, Y_e, Y_{ν_e}, Y_μ, and Y_{ν_μ} by solving Eqs. (10a)–(10f) simultaneously. We carry out the calculations up to $t_{\rm pb} = 1.1$ s in multiple time steps. For each step, we require that the results have numerically converged (with differences less than 1% when the calculations are repeated with half the step size). We have also checked that throughout the

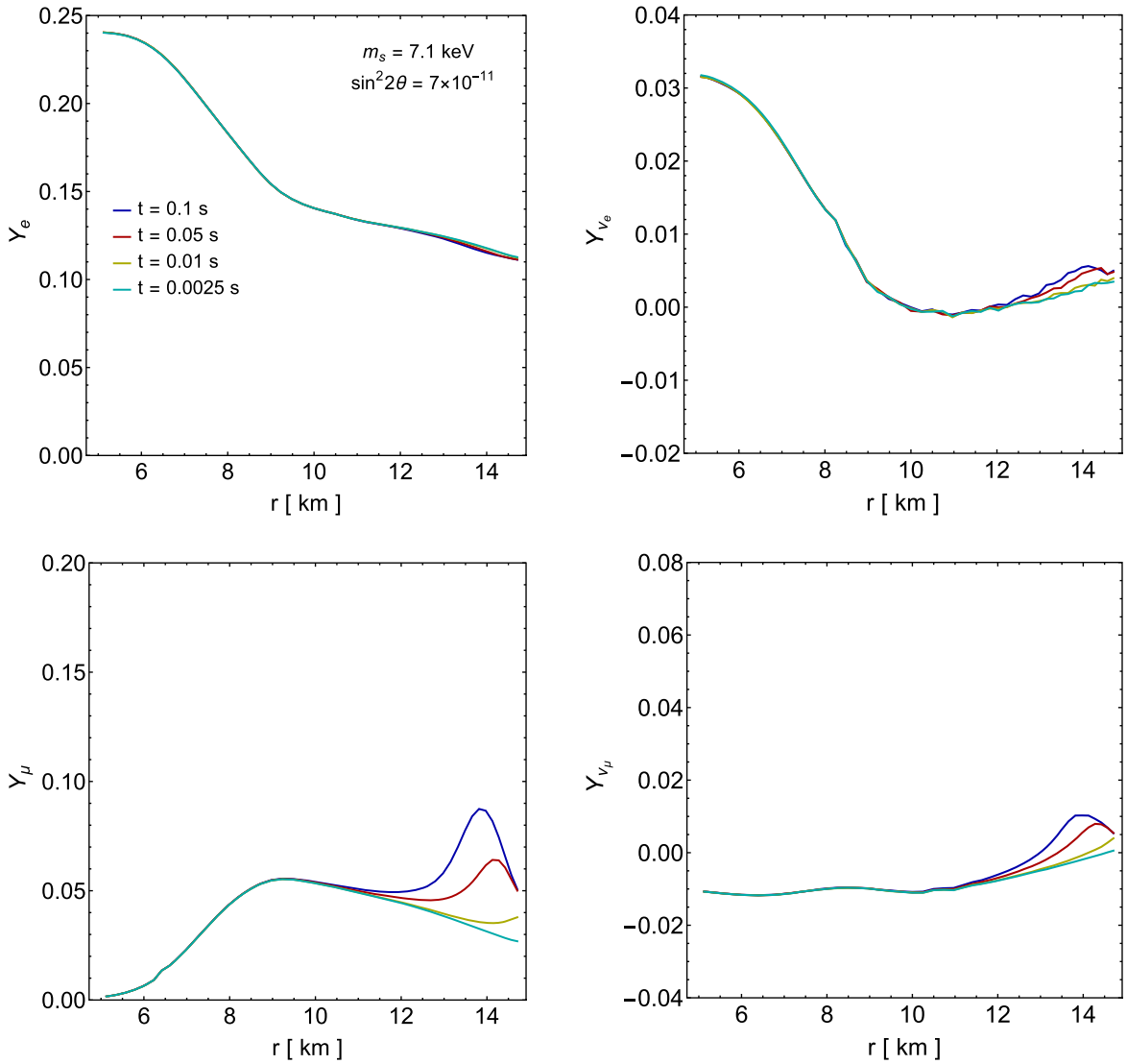

FIG. 3. Evolution of Y_e, Y_{ν_e}, Y_μ, and Y_{ν_μ} as functions of radius r and time t for $m_s = 7.1$ keV and $\sin^2 2\theta = 7 \times 10^{-11}$. Diffusion of Y_{ν_e} and Y_{ν_μ} is ignored.

calculations, the changes in the total energy density and pressure of each radial zone are small (always less than 10% but typically a few percentage or less) as compared to the initial values of these quantities. For illustration, we show the results for $t_{\rm pb} = 1.0025$, 1.01, 1.05, and 1.1 s.

We take $\delta m^2 \approx m_s^2$ with $m_s = 7.1$ keV and $\sin^2 2\theta = 7 \times 10^{-11}$, which are suggested by interpreting the x-ray line emission near 3.55 keV from galaxy clusters as due to sterile neutrino decay [42,43]. For comparison, we use $m_s = 10$ keV and $\sin^2 2\theta = 10^{-12}$, which are chosen for sterile neutrinos to make up all the dark matter [8,11]. For convenience, hereafter we refer to the two adopted sets of mixing parameters by the corresponding m_s values. Using the rates Γ_{L_e} and Γ_{L_μ} in Eqs. (11a) and (11b), we show the evolution of Y_e (top left), Y_{ν_e} (top right), Y_μ (bottom left), and Y_{ν_μ} (bottom right) as functions of radius r and time t in Figs. 3 and 4 for $m_s = 7.1$ and 10 keV, respectively. The evolution of Y_n and Y_p (not shown) can be obtained from that of Y_e and Y_μ through Eqs. (10a) and (10b).

As shown in Figs. 3 and 4, there is little evolution of Y_e; the evolution of Y_{ν_e} is less than that of Y_{ν_μ}, and the evolution of Y_μ is the largest. This comparison is reflected by changes of the corresponding chemical potentials. For illustration, we show in the left (right) panel of Fig. 5 the evolution of the chemical potentials μ_e, μ_{ν_e}, μ_μ, and μ_{ν_μ} for the zone at $r = 14.1$ km for $m_s = 7.1\,(10)$ keV. It can be seen that the changes $|\Delta\mu_e|$ and $|\Delta\mu_{\nu_e}|$ are much smaller than $|\Delta\mu_{\nu_\mu}|$ and $|\Delta\mu_\mu|$, which along with $(\mu_e - \mu_{\nu_e}) - (\mu_\mu - \mu_{\nu_\mu}) = 0$ for chemical equilibrium [see Eqs. (10c) and (10d)], gives $\Delta\mu_\mu \sim \Delta\mu_{\nu_\mu}$. For the conditions in the PNS, the increase of Y_μ with μ_μ is much steeper than that of Y_{ν_μ} with μ_{ν_μ} because of the muon rest mass (see Fig. 6). Therefore, the modest increase of Y_{ν_μ} mainly due to

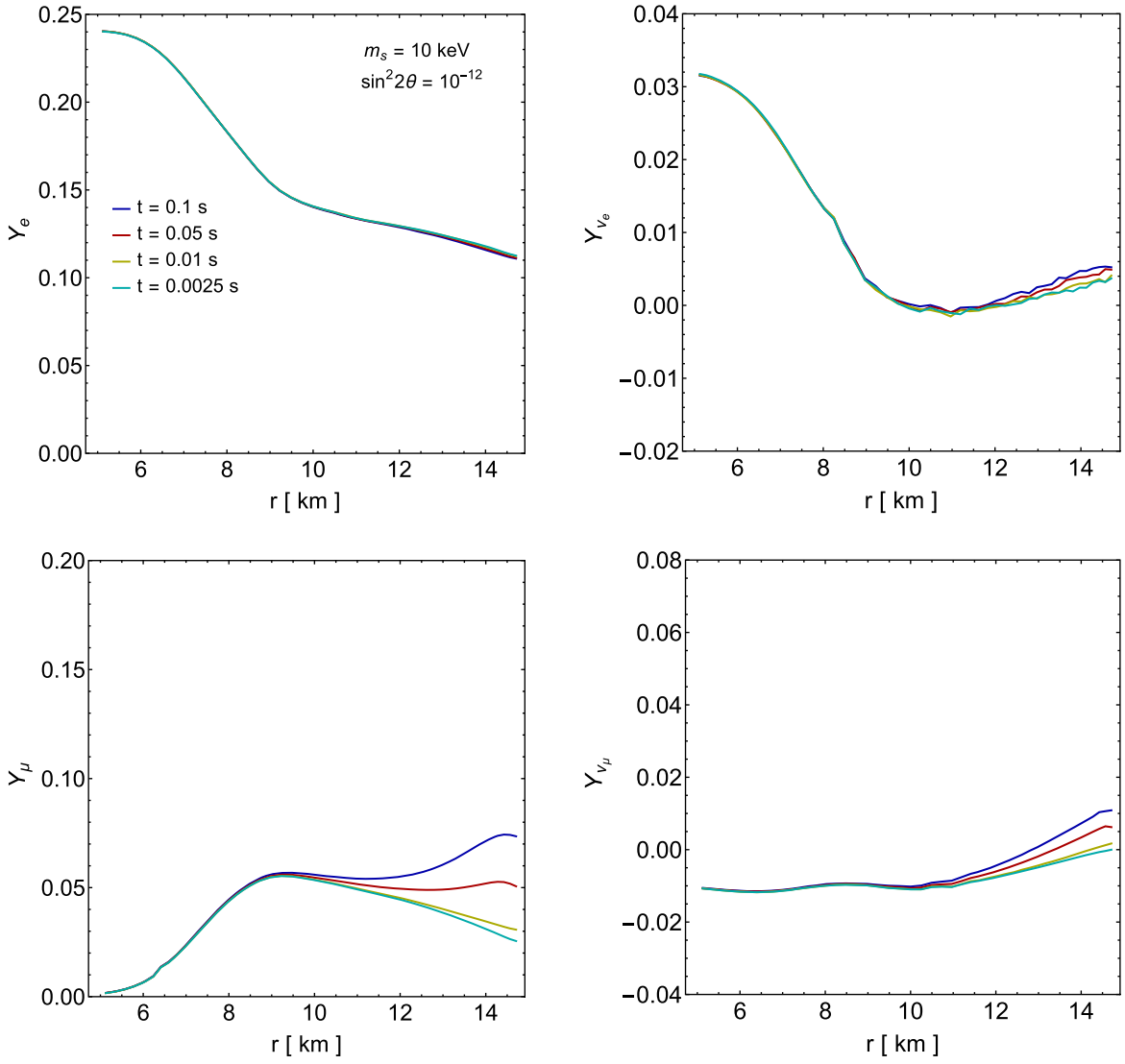

FIG. 4. Similar to Fig. 3, but for $m_s = 10$ keV and $\sin^2 2\theta = 10^{-12}$.

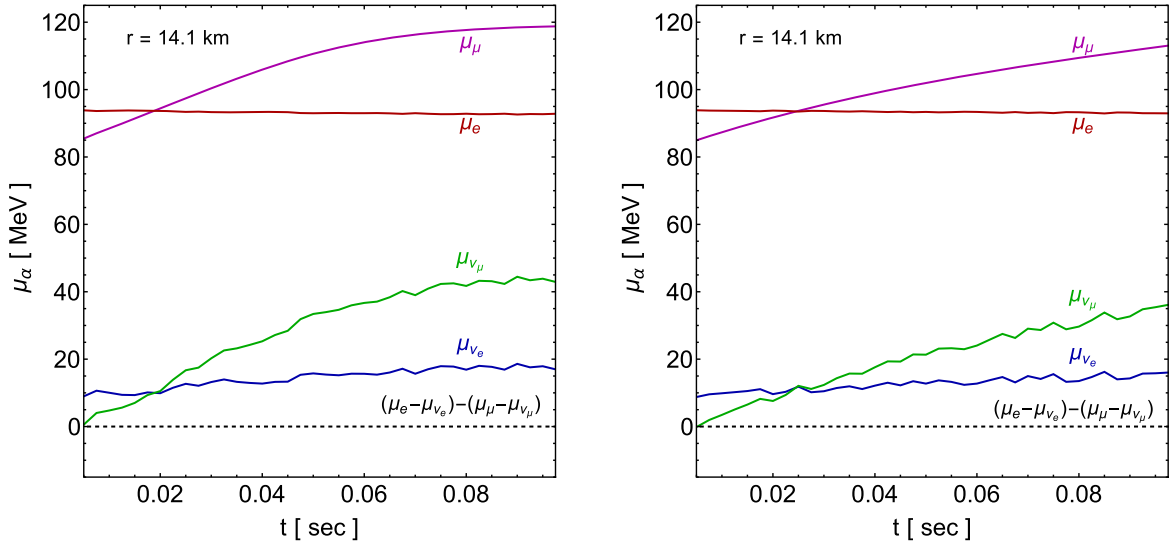

FIG. 5. Evolution of the chemical potentials μ_e, μ_{ν_e}, μ_μ, and μ_{ν_μ} as functions of time t for the zone at $r = 14.1$ km. The left (right) panel shows the results for $m_s = 7.1(10)$ keV and $\sin^2 2\theta = 7 \times 10^{-11}(10^{-12})$. Chemical equilibrium among the relevant particles gives $(\mu_e - \mu_{\nu_e}) - (\mu_\mu - \mu_{\nu_\mu}) = 0$.

the MSW conversion of $\bar{\nu}_\mu$ into $\bar{\nu}_s$ gives rise to the substantial increase of Y_μ through chemical equilibrium.

To understand better the dominant production of sterile neutrinos through the MSW conversion of $\bar{\nu}_\mu$ into $\bar{\nu}_s$, we show the corresponding rate $\dot{Y}^{\rm MSW}_{\nu_\mu}$ for change in Y_{ν_μ} as functions of radius r and time t in the top panels of Fig. 7. Initially $\dot{Y}^{\rm MSW}_{\nu_\mu}$ increases with radius as $\bar{\nu}_\mu$ of higher energy go through MSW resonances at larger radii (bottom panels of Fig. 7). The resulting production and escape of $\bar{\nu}_s$ change Y_{ν_μ} directly and alter Y_μ, Y_e, Y_{ν_e}, Y_n, and Y_p through chemical equilibrium. Consequently, the potential $V_{\bar{\nu}}$ is changed, which in turn affects the subsequent MSW conversion of $\bar{\nu}_\mu$ into $\bar{\nu}_s$. These feedback effects are clearly shown in Fig. 7. At the same radius, the resonant energy $E_R \approx \delta m^2/(2V_{\bar{\nu}})$ increases with time, mostly due to the increase of Y_μ and hence decrease of $V_{\bar{\nu}} \sim \sqrt{2} G_F n_b[(Y_n/2) - Y_\mu]$. The evolution of $\dot{Y}^{\rm MSW}_{\nu_\mu}$ is more complicated because it depends on both the resonant energy and the evolving energy

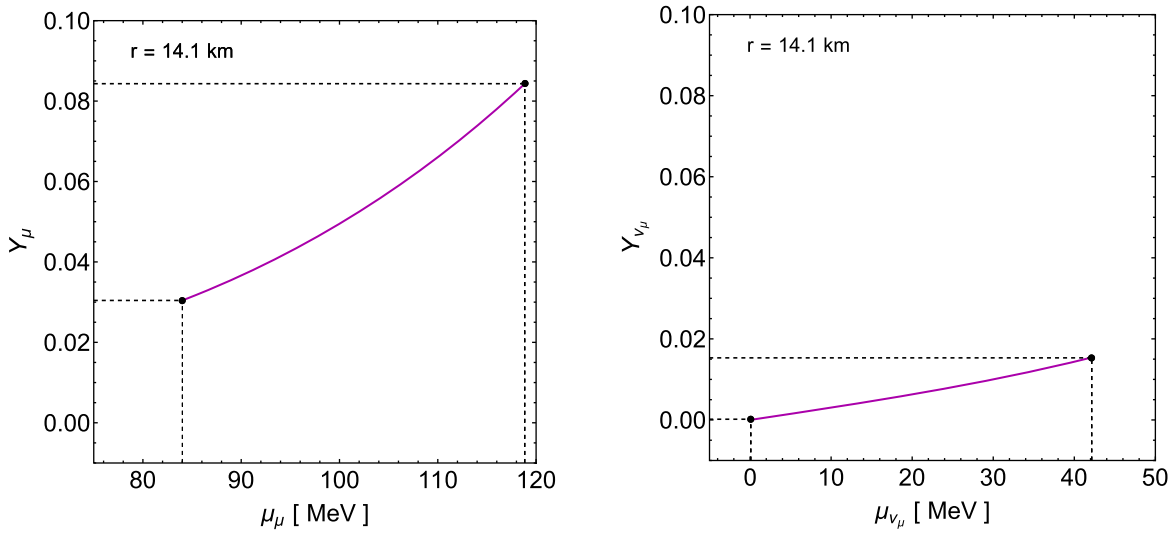

FIG. 6. Net number fractions Y_μ (left panel) and Y_{ν_μ} (right panel) as functions of chemical potentials μ_μ and μ_{ν_μ}, respectively, for the zone at $r = 14.1$ km with $T = 28.9$ MeV and $\rho = 9.99 \times 10^{13}$ g cm^{-3}. The solid points indicate the values at $t_{\rm pb} = 1$ and 1.1 s from the calculations without diffusion of Y_{ν_e} and Y_{ν_μ} for $m_s = 7.1$ keV and $\sin^2 2\theta = 7 \times 10^{-11}$. Because of the muon rest mass, the increase of Y_μ with μ_μ is much steeper than that of Y_{ν_μ} with μ_{ν_μ}. Therefore, similar increases of μ_μ and μ_{ν_μ} due to chemical equilibrium result in an increase of Y_μ much larger than that of Y_{ν_μ}.

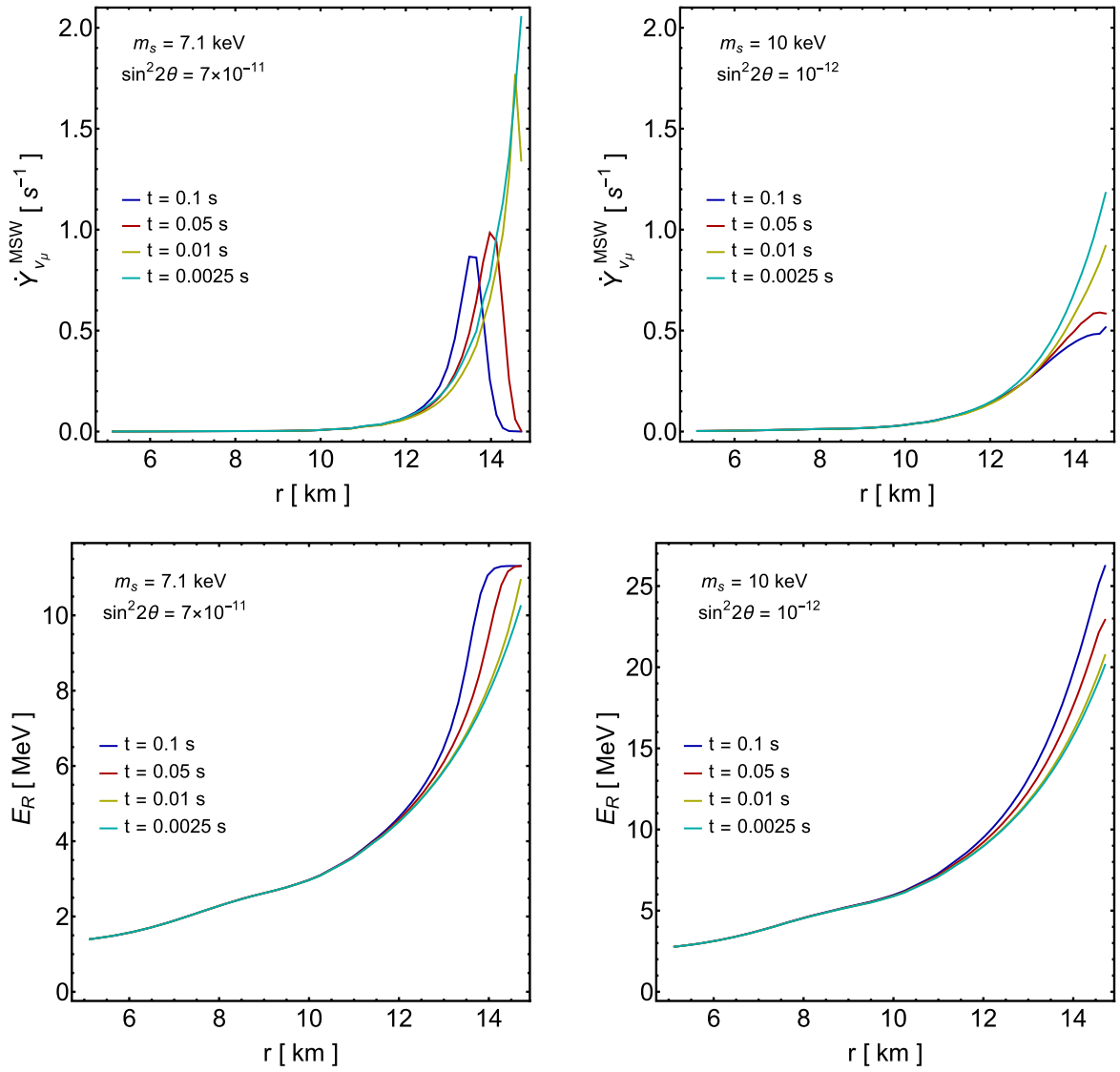

FIG. 7. Evolution of the rate $\dot{Y}^{\rm MSW}_{\nu_\mu}$ and the resonant energy E_R as functions of radius r and time t for the MSW conversion of $\bar{\nu}_\mu$ into $\bar{\nu}_s$ with $(m_s/\text{keV}, \sin^2 2\theta) = (7.1, 7\times10^{-11})$ (left panels) and $(10, 10^{-12})$ (right panels). Diffusion of Y_{ν_e} and Y_{ν_μ} is ignored.

distribution of $\bar{\nu}_\mu$ (due to the change of μ_{ν_μ}). The general tendency is that $\dot{Y}^{\rm MSW}_{\nu_\mu}$ decreases with time, i.e., the feedback of ν_μ-ν_s and $\bar{\nu}_\mu$-$\bar{\nu}_s$ mixing tends to turn off such mixing (e.g., [28,32,35]). While the cases of $m_s = 7.1$ and 10 keV are similar, the relevant resonant energy is higher (due to a higher δm^2), and the corresponding MSW conversion is less adiabatic (mostly due to a much smaller $\sin^2 2\theta$) for the latter. Consequently, the evolution of Y_μ is significantly different for the two cases (the differences in the evolution of Y_{ν_e} and Y_{ν_μ} are also noticeable; see Figs. 3 and 4).

V. DISCUSSION AND CONCLUSIONS

We have presented the effects of ν_μ-ν_s and $\bar{\nu}_\mu$-$\bar{\nu}_s$ mixing with $\delta m^2 \sim 10^2$ keV^2 in the PNS. In addition to the obvious feedback on the ν_μ lepton number, we have included for the first time, the feedback on the composition of the PNS. For our adopted mixing parameters, which are consistent with current constraints, we find that sterile neutrinos are dominantly produced through the MSW conversion of $\bar{\nu}_\mu$ into $\bar{\nu}_s$. This production and the subsequent escape of $\bar{\nu}_s$ increase the ν_μ lepton number, which in turn enhances muonization mainly through $\nu_\mu + n \to p + \mu^-$ and changes the number fractions Y_e, Y_{ν_e}, Y_p, and Y_n through chemical equilibrium.

In our adopted CCSN model [38], Y_μ reaches the peak value of 0.0566 at $r = 8.97$ km at $t_{\rm pb} = 1$ s with standard physics. By including ν_μ-ν_s and $\bar{\nu}_\mu$-$\bar{\nu}_s$ mixing with $\delta m^2 \approx m_s^2 \sim 10^2$ keV^2, we have shown that enhanced muonization occurs in that model at larger radii ($r \sim 12$–14.7 km) beyond the original peak of Y_μ (Figs. 3 and 4). This

enhancement is driven by the MSW resonances of $\bar{\nu}_\mu$ with $E_R \sim 4$–10 (8–20) MeV for $m_s = 7.1$ (10) keV (Fig. 7).

We have ignored diffusion of Y_{ν_e} and Y_{ν_μ} in our calculations. Based on our adopted CCSN model with standard physics but with detailed treatment of such diffusion, the PNS is contracting between $t_{\rm pb} = 1$ and 1.25 s, and the resulting change in the density profile and more importantly, that in the temperature profile are most likely the dominant factors driving the evolution of composition profiles (see Fig. 2). However, changes of Y_{ν_e}, Y_{ν_μ}, and especially Y_μ found in our calculations (assuming fixed temperature and density profiles over a duration of 0.1 s) are qualitatively different from those in the CCSN model with standard physics (see Figs. 3 and 4). Further, in the region of $r \sim 12$–14.7 km, the increase of Y_μ obtained from our calculations quantitatively exceeds the corresponding change in the standard CCSN model. Therefore, we regard enhanced muonization as a qualitatively robust result from ν_μ-ν_s and $\bar{\nu}_\mu$-$\bar{\nu}_s$ mixing with $\delta m^2 \sim 10^2$ keV^2 in the PNS, and expect that it still occurs when such mixing is incorporated in CCSN simulations. Such self-consistent simulations should be carried out to assess quantitatively the effects discussed here.

We have chosen to study the epoch of $t_{\rm pb} \approx 1$ s because the corresponding temperature and density profiles change so slowly that we can ignore such changes when studying the effects of ν_μ-ν_s and $\bar{\nu}_\mu$-$\bar{\nu}_s$ mixing for a duration of 0.1 s. On the other hand, the PNS conditions do not differ greatly for $t_{\rm pb} \sim 0.4$–2 s, and the conditions at $t_{\rm pb} \sim 0.1$ s are also not qualitatively different, which suggests that our results can be extended to earlier and later times. With the help of muonization, neutrino-driven explosion occurs at $t_{\rm pb} \sim 0.24$ s in our adopted CCSN model [38]. We expect that when ν_μ-ν_s and $\bar{\nu}_\mu$-$\bar{\nu}_s$ mixing with $\delta m^2 \sim 10^2$ keV^2 is included in CCSN simulations, enhanced muonization similar to that found here would occur at the explosion epoch, potentially making the explosion easier. However, due to the intrinsically dynamic nature of the explosion, a definitive conclusion can only be reached by implementing such mixing in CCSN simulations.

Subsequent to the explosion, cooling of the PNS by active neutrino emission lasts up to ~10 s. Active neutrinos emitted from the PNS drive winds (e.g., [44]) that may be an important source for heavy element nucleosynthesis (e.g., [45]). Further, this nucleosynthesis may be affected by collective oscillations of active neutrinos (see, e.g., [46] for a recent review) that are sensitive to the net lepton number carried by ν_μ and $\bar{\nu}_\mu$ fluxes [47]. With enhanced muonization due to ν_μ-ν_s and $\bar{\nu}_\mu$-$\bar{\nu}_s$ mixing in the PNS, we expect that a significant net ν_μ lepton number is emitted from the PNS, but note that the quantitative characteristics of active neutrino emission can only be obtained by including such mixing in CCSN simulations. We will explore the implications of enhanced muonization for the CCSN dynamics and collective neutrino oscillations in future works.

ACKNOWLEDGMENTS

We sincerely thank Daniel Kresse and Thomas Janka for providing the CCSN model used in this work. This work was supported in part by the National Science Foundation (Grant No. PHY-2020275), the Heising-Simons Foundation (Grant No. 2017-228), and the U.S. Department of Energy (Grant No. DE-FG02-87ER40328).

APPENDIX: CHARGED-CURRENT WEAK REACTION RATES

Under the so-called elastic approximation (the nucleons carry the same momentum), the rate for $\nu_e + n \to p + e^-$ is given by

$$\Gamma_{\nu_e n} = \frac{1}{n_b Y_n} \int_0^\infty \frac{p^2 dp}{\pi^2} f_n(E_n)[1 - f_p(E_p)] \times \int_0^\infty \frac{E_{\nu_e}^2 dE_{\nu_e}}{2\pi^2} f_{\nu_e}(E_{\nu_e})[1 - f_{e^-}(E_{e^-})]\sigma_{\nu_e n}(E_{e^-}), \quad \text{(A1)}$$

where

$$\sigma_{\nu_e n}(E_{e^-}) = \frac{G_F^2}{\pi} \cos^2\theta_c (f^2 + 3g^2) E_{e^-} p_{e^-} \quad \text{(A2)}$$

is the cross section, θ_c denotes the Cabibbo angle with $\cos^2\theta_c \approx 0.95$, $f = 1$ and $g \approx 1.27$ are weak coupling constants,

$$f_\alpha(E_\alpha) = \frac{1}{\exp[(E_\alpha - \mu_\alpha)/T] + 1} \quad \text{(A3)}$$

is the occupation number of species α with $\alpha = n$, p, ν_e, and e^-, and the chemical potential μ_α includes the rest mass m_α of the species. In the above equations,

$$E_{n,p} = \sqrt{p^2 + (m^*_{n,p})^2} - m^*_{n,p} + m_{n,p} + U_{n,p}, \quad \text{(A4)}$$

$$E_{e^-} = \sqrt{p_{e^-}^2 + m_e^2} \quad \text{(A5)}$$

$$= E_{\nu_e} + m_n - m_p + U_n - U_p, \quad \text{(A6)}$$

where for example, m_n^* and U_n are the effective mass and potential, respectively, for neutrons in the PNS (e.g., [46]).

The rate $\Gamma_{\nu_\mu n}$ for $\nu_\mu + n \to p + \mu^-$ can be obtained by replacing quantities for ν_e (e^-) with those for ν_μ (μ^-) in the equations for $\Gamma_{\nu_e n}$.

The rate for $\bar{\nu}_e + p \to n + e^+$ is given by

$$\Gamma_{\bar{\nu}_e p} = \frac{1}{n_b Y_p} \int_0^\infty \frac{p^2 dp}{\pi^2} f_p(E_p)[1 - f_n(E_n)] \times \int_{E^{\rm th}_{\bar{\nu}_e}}^\infty \frac{E^2_{\bar{\nu}_e} dE_{\bar{\nu}_e}}{2\pi^2} f_{\bar{\nu}_e}(E_{\bar{\nu}_e})[1 - f_{e^+}(E_{e^+})]\sigma_{\bar{\nu}_e p}(E_{e^+}), \tag{A7}$$

where $\sigma_{\bar{\nu}_e p}(E_{e^+})$ can be obtained by replacing E_{e^-} (p_{e^-}) with E_{e^+} (p_{e^+}) in Eq. (A2) for $\sigma_{\nu_e n}(E_{e^-})$,

$$E_{e^+} = E_{\bar{\nu}_e} + m_p - m_n + U_p - U_n, \tag{A8}$$

and $E^{\rm th}_{\bar{\nu}_e}$ corresponds to $E_{e^+} = m_e$. Note that in the occupation number $f_{\bar{\alpha}}(E_{\bar{\alpha}})$ for an antiparticle $\bar{\alpha}$, the chemical potential is $\mu_{\bar{\alpha}} = -\mu_\alpha$.

The rate $\Gamma_{\bar{\nu}_\mu p}$ for $\bar{\nu}_\mu + p \to n + \mu^+$ can be obtained by replacing quantities for $\bar{\nu}_e$ (e^+) with those for $\bar{\nu}_\mu$ (μ^+) in the equations for $\Gamma_{\bar{\nu}_e p}$.

By detailed balance, the rates for $e^+ + n \to p + \bar{\nu}_e$, $\mu^+ + n \to p + \bar{\nu}_\mu$, $e^- + p \to n + \nu_e$, and $\mu^- + p \to n + \nu_\mu$ are given by

$$\Gamma_{e^+ n} = \frac{Y_p}{Y_n}\Gamma_{\bar{\nu}_e p} \exp\left(\frac{\mu_{\nu_e} + \mu_n - \mu_p - \mu_e}{T}\right), \tag{A9}$$

$$\Gamma_{\mu^+ n} = \frac{Y_p}{Y_n}\Gamma_{\bar{\nu}_\mu p} \exp\left(\frac{\mu_{\nu_\mu} + \mu_n - \mu_p - \mu_\mu}{T}\right), \tag{A10}$$

$$\Gamma_{e^- p} = \frac{Y_n}{Y_p}\Gamma_{\nu_e n} \exp\left(\frac{\mu_e + \mu_p - \mu_n - \mu_{\nu_e}}{T}\right), \tag{A11}$$

$$\Gamma_{\mu^- p} = \frac{Y_n}{Y_p}\Gamma_{\nu_\mu n} \exp\left(\frac{\mu_\mu + \mu_p - \mu_n - \mu_{\nu_\mu}}{T}\right). \tag{A12}$$

The exponential factors in the above equations reduce to unity when the relevant particles are in chemical equilibrium. We have checked that the charged-current weak reaction rates are sufficiently fast, and therefore, chemical equilibrium is achieved to very good approximation.

[1] A. Kusenko, Sterile neutrinos: The dark side of the light fermions, Phys. Rep. **481**, 1 (2009).
[2] M. Drewes *et al.*, A white paper on keV sterile neutrino dark matter, J. Cosmol. Astropart. Phys. 01 (2017) 025.
[3] K. N. Abazajian, Sterile neutrinos in cosmology, Phys. Rep. **711–712**, 1 (2017).
[4] A. Boyarsky, M. Drewes, T. Lasserre, S. Mertens, and O. Ruchayskiy, Sterile neutrino dark matter, Prog. Part. Nucl. Phys. **104**, 1 (2019).
[5] B. Dasgupta and J. Kopp, Sterile neutrinos, Phys. Rep. **928**, 1 (2021).
[6] K. Abazajian, G. M. Fuller, and W. H. Tucker, Direct detection of warm dark matter in the x-ray, Astrophys. J. **562**, 593 (2001).
[7] A. Boyarsky, D. Malyshev, A. Neronov, and O. Ruchayskiy, Constraining DM properties with SPI, Mon. Not. R. Astron. Soc. **387**, 1345 (2008).
[8] K. C. Y. Ng, B. M. Roach, K. Perez, J. F. Beacom, S. Horiuchi, R. Krivonos, and D. R. Wik, New constraints on sterile neutrino dark matter from *NuSTAR* M31 observations, Phys. Rev. D **99**, 083005 (2019).
[9] B. M. Roach, K. C. Y. Ng, K. Perez, J. F. Beacom, S. Horiuchi, R. Krivonos, and D. R. Wik, NuSTAR tests of sterile-neutrino dark matter: New Galactic bulge observations and combined impact, Phys. Rev. D **101**, 103011 (2020).
[10] J. W. Foster, M. Kongsore, C. Dessert, Y. Park, N. L. Rodd, K. Cranmer, and B. R. Safdi, Deep search for decaying dark matter with XMM-Newton blank-sky observations, Phys. Rev. Lett. **127**, 051101 (2021).
[11] B. M. Roach, S. Rossland, K. C. Y. Ng, K. Perez, J. F. Beacom, B. W. Grefenstette, S. Horiuchi, R. Krivonos, and D. R. Wik, Long-exposure NuSTAR constraints on decaying dark matter in the Galactic halo, Phys. Rev. D **107**, 023009 (2023).
[12] S. Tremaine and J. E. Gunn, Dynamical role of light neutral leptons in cosmology, Phys. Rev. Lett. **42**, 407 (1979).
[13] A. Boyarsky, O. Ruchayskiy, and D. Iakubovskyi, A lower bound on the mass of dark matter particles, J. Cosmol. Astropart. Phys. 03 (2009) 005.
[14] D. Gorbunov, A. Khmelnitsky, and V. Rubakov, Constraining sterile neutrino dark matter by phase-space density observations, J. Cosmol. Astropart. Phys. 10 (2008) 041.
[15] C. Di Paolo, F. Nesti, and F. L. Villante, Phase space mass bound for fermionic dark matter from dwarf spheroidal galaxies, Mon. Not. R. Astron. Soc. **475**, 5385 (2018).
[16] A. Boyarsky, J. Lesgourgues, O. Ruchayskiy, and M. Viel, Lyman-alpha constraints on warm and on warm-plus-cold dark matter models, J. Cosmol. Astropart. Phys. 05 (2009) 012.
[17] V. Iršič *et al.*, New constraints on the free-streaming of warm dark matter from intermediate and small scale Lyman-α forest data, Phys. Rev. D **96**, 023522 (2017).
[18] I. A. Zelko, T. Treu, K. N. Abazajian, D. Gilman, A. J. Benson, S. Birrer, A. M. Nierenberg, and A. Kusenko, Constraints on sterile neutrino models from strong gravitational lensing, Milky Way satellites, and the Lyman-α forest, Phys. Rev. Lett. **129**, 191301 (2022).
[19] P. F. Smith, Proposed experiments to detect keV range sterile neutrinos using energy-momentum reconstruction

of beta decay or K-capture events, New J. Phys. **21**, 053022 (2019).
[20] S. Mertens *et al.* (KATRIN Collaboration), A novel detector system for KATRIN to search for keV-scale sterile neutrinos, J. Phys. G **46**, 065203 (2019).
[21] C. Benso, V. Brdar, M. Lindner, and W. Rodejohann, Prospects for finding sterile neutrino dark matter at KATRIN, Phys. Rev. D **100**, 115035 (2019).
[22] A. B. Balantekin, G. M. Fuller, A. Ray, and A. M. Suliga, Probing self-interacting sterile neutrino dark matter with the diffuse supernova neutrino background, Phys. Rev. D **108**, 123011 (2023).
[23] X. Shi and G. Sigl, A type II supernovae constraint on electron-neutrino—sterile-neutrino mixing, Phys. Lett. B **323**, 360 (1994).
[24] H. Nunokawa, J. T. Peltoniemi, A. Rossi, and J. W. F. Valle, Supernova bounds on resonant active sterile neutrino conversions, Phys. Rev. D **56**, 1704 (1997).
[25] J. Hidaka and G. M. Fuller, Dark matter sterile neutrinos in stellar collapse: Alteration of energy/lepton number transport and a mechanism for supernova explosion enhancement, Phys. Rev. D **74**, 125015 (2006).
[26] J. Hidaka and G. M. Fuller, Sterile neutrino-enhanced supernova explosions, Phys. Rev. D **76**, 083516 (2007).
[27] G. Raffelt and G. Sigl, Neutrino flavor conversion in a supernova core, Astropart. Phys. **1**, 165 (1993).
[28] G. G. Raffelt and S. Zhou, Supernova bound on keV-mass sterile neutrinos reexamined, Phys. Rev. D **83**, 093014 (2011).
[29] M. L. Warren, M. Meixner, G. Mathews, J. Hidaka, and T. Kajino, Sterile neutrino oscillations in core-collapse supernovae, Phys. Rev. D **90**, 103007 (2014).
[30] M. Warren, G. J. Mathews, M. Meixner, J. Hidaka, and T. Kajino, Impact of sterile neutrino dark matter on core-collapse supernovae, Int. J. Mod. Phys. A **31**, 1650137 (2016).
[31] C. A. Argüelles, V. Brdar, and J. Kopp, Production of keV sterile neutrinos in supernovae: New constraints and gamma-ray observables, Phys. Rev. D **99**, 043012 (2019).
[32] A. M. Suliga, I. Tamborra, and M.-R. Wu, Tau lepton asymmetry by sterile neutrino emission—moving beyond one-zone supernova models, J. Cosmol. Astropart. Phys. 12 (2019) 019.
[33] A. M. Suliga, I. Tamborra, and M.-R. Wu, Lifting the core-collapse supernova bounds on keV-mass sterile neutrinos, J. Cosmol. Astropart. Phys. 08 (**2020**) 018.
[34] V. Syvolap, O. Ruchayskiy, and A. Boyarsky, Resonance production of kev sterile neutrinos in core-collapse supernovae and lepton number diffusion, Phys. Rev. D **106**, 015017 (2022).
[35] A. Ray and Y.-Z. Qian, Evolution of tau-neutrino lepton number in protoneutron stars due to active-sterile neutrino mixing, Phys. Rev. D **108**, 063025 (2023).
[36] P. Carenza, G. Lucente, L. Mastrototaro, A. Mirizzi, and P. D. Serpico, Comprehensive constraints on heavy sterile neutrinos from core-collapse supernovae, Phys. Rev. D **109**, 063010 (2024).
[37] G. Chauhan, S. Horiuchi, P. Huber, and I. M. Shoemaker, Low-energy supernovae bounds on sterile neutrinos, arXiv:2309.05860.
[38] R. Bollig, H. T. Janka, A. Lohs, G. Martínez-Pinedo, C. J. Horowitz, and T. Melson, Muon creation in supernova matter facilitates neutrino-driven explosions, Phys. Rev. Lett. **119**, 242702 (2017).
[39] S. P. Mikheyev and A. Y. Smirnov, Resonance enhancement of oscillations in matter and solar neutrino spectroscopy, Sov. J. Nucl. Phys. **42**, 913 (1985).
[40] L. Wolfenstein, Neutrino oscillations in matter, Phys. Rev. D **17**, 2369 (1978).
[41] https://wwwmpa.mpa-garching.mpg.de/ccsnarchive/.
[42] E. Bulbul, M. Markevitch, A. Foster, R. K. Smith, M. Loewenstein, and S. W. Randall, Detection of an unidentified emission line in the stacked x-ray spectrum of galaxy clusters, Astrophys. J. **789**, 13 (2014).
[43] A. Boyarsky, O. Ruchayskiy, D. Iakubovskyi, and J. Franse, Unidentified line in x-ray spectra of the Andromeda Galaxy and Perseus Galaxy cluster, Phys. Rev. Lett. **113**, 251301 (2014).
[44] Y. Z. Qian and S. E. Woosley, Nucleosynthesis in neutrino-driven winds. I. The physical conditions, Astrophys. J. **471**, 331 (1996).
[45] R. D. Hoffman, S. E. Woosley, and Y. Z. Qian, Nucleosynthesis in neutrino-driven winds. II. Implications for heavy element synthesis, Astrophys. J. **482**, 951 (1997).
[46] T. Fischer, G. Guo, K. Langanke, G. Martínez-Pinedo, Y.-Z. Qian, and M.-R. Wu, Neutrinos and nucleosynthesis of elements, Prog. Part. Nucl. Phys. **137**, 104107 (2024).
[47] F. Capozzi, M. Chakraborty, S. Chakraborty, and M. Sen, Mu-tau neutrinos: Influencing fast flavor conversions in supernovae, Phys. Rev. Lett. **125**, 251801 (2020).